Research Square

Preprints are preliminary reports that have not undergone peer review.
They should not be considered conclusive, used to inform clinical practice,
or referenced by the media as validated information.

2D MXenes: the lowest-emissivity black materials

Yang Li
The Hong Kong University of Science and Technology
Cheng Xiong
The Hong Kong University of Science and Technology
He Huang
The Hong Kong University of Science and Technology
Xudong Peng
The Hong Kong University of Science and Technology
Meng Li
The Hong Kong University of Science and Technology
Deqing Mei
Zhejiang University
Gongze Liu
The Hong Kong University of Science and Technology
Maochun Wu
The Hong Kong University of Science and Technology
Tianshou Zhao
The Hong Kong University of Science and Technology https://orcid.org/0000-0003-4825-2381
Baoling Huang (mebhuang@ust.hk)
The Hong Kong University of Science and Technology

Article

Keywords: black material, low infrared absorption/emission, 2D MXenes

Posted Date: May 18th, 2021

DOI: https://doi.org/10.21203/rs.3.rs-149825/v1

License: This work is licensed under a Creative Commons Attribution 4.0 International License.
Read Full License

Abstract

Black materials with low infrared absorption/emission are rare in nature but highly desired in numerous areas, such as solar-thermal energy harvesting, infrared camouflage, and anti-counterfeiting. Due to the lack of spectral selectivity in intrinsic materials, such counter-intuitive properties are generally realized by constructing complicated subwavelength artificial nanostructures with precise nanofabrication techniques. Here, we report that 2D Ti3C2Tx MXenes embrace both a low emissivity (down to 10%) and a high solar absorptance (up to 90%), yielding the best spectral selectivity (8.2) and the highest solar-thermal efficiency among the reported intrinsic solar absorbing materials. We demonstrate their appealing potentials in the aforementioned areas. Moreover, the spectral selectivity relies on both the nanoflake orientations and terminal groups, providing great tunability. First-principles calculations suggest more potential low-emissivity MXenes such as Ti2CTx, Nb2CTx, and V2CTx. This work opens the avenue to further exploration of a family of low-emissivity black materials with over 70 members.

Main Text

Black materials with intrinsically low mid-IR emissivity are scarce but of great significance for many areas, such as solar energy harvesting[1-4], thermal insulation[5,6], and multispectral camouflage[7,8]. For instance, in solar-thermal energy conversion systems, to maximize the conversion efficiency, ideal solar absorbing black materials should show perfect absorption over the solar spectrum (0.3-2.5 μm), but simultaneously ultralow mid-IR absorption/emission (2.5-20 μm) to suppress enormous re-radiative heat dissipation (e.g. 0.68 kW m^{-2} @ 100 °C, 0.68 sun), known as selective solar absorption[1-4,9]. Intuitively, under the same solar irradiance, the low-emissivity absorbing materials reach much higher temperatures than those blackbody materials, such as carbon-based materials[10-12], black polymers[13], and black oxides[14-16]. The more generated thermal energy and larger temperature rises are highly beneficial for a lot of heat-driven applications including passive heating[17], anti-icing/deicing[18], steam generation[1,4], low-temperature batteries[19], catalysis[9], actuators[20], and electricity generation[21]. Moreover, even with higher surface temperatures, low-emissivity black materials have the counter-intuitive ability to conceal themselves from IR detection due to their limited thermal radiation, showing great potential in multispectral (IR and visible) camouflage assisted by their dark colors[8,22].

Due to the lack of intrinsic materials with satisfactory spectral selectivity in nature, great efforts have been made in designing subwavelength metamaterials or metasurfaces with exotic optical properties through various light manipulation strategies, including photonic crystals[23,24], plasmon resonances[3,4,25], and interference effects[26-29]. However, there are several limitations in these artificial low-emissivity absorbers based on structural engineering in nanoscale. First, most of these selective absorbers have to employ both additional reflectors (metals in most cases) to provide strong IR reflection and anti-reflection coating (metal oxides in most cases). Second, they are typically pore-free dense structures with rigid substrates. These two features significantly hinder the diversity of their application scenarios. Third, the properties of these subwavelength absorbers are extremely sensitive to the feature size of nanostructures,

and therefore precise lithography or high-vacuum deposition techniques generally have to be used in their fabrication, which inherently restricts their cost reduction. For these reasons, it is preferable if there was a flexible intrinsic material with strong, broadband solar absorption but low IR emissivity. In fact, prior to the exploration of metamaterials/metasurfaces, materials with intrinsic spectral selectivity such as W, HfC, SnO_2, In_2O_3, ZrB_2, and TiB_2 were investigated[30-32], but their innate solar absorptance (<70%) and spectral selectivity were generally well below the generally desired threshold value for efficient solar harvesting (Supplementary Table 1). The lack of ideal intrinsic low-emissivity black materials has been a long-standing challenge for decades[21,30].

In this context, we resorted to a new family of two-dimensional (2D) materials, MXenes, composed of transitional metal carbides and nitrides. Since they were first reported in 2011[33], MXenes have brought substantial benefits and new opportunities to a variety of areas ranging from energy storage[34,35], and catalysis[36] to electromagnetic shielding[37,38], and photothermal conversion[39-41]. Specifically, the outstanding ability of $Ti_3C_2T_x$ (T denotes the -O-, -OH, -F and other terminal groups) MXenes in electromagnetic wave absorption has enabled both the electromagnetic interference shield effects (in the microwave region)[37,38] and photothermal effects (in the visible and near-IR regions)[39-41]. However, the interaction between the MXenes and electromagnetic waves in the mid-IR region (>2.5 μm), which dominates the radiative heat transfer near room temperature, is rarely explored.

In this study, for the first time, we discovered that unlike the strong absorption in visible, near-IR, and microwave regions, the black $Ti_3C_2T_x$ MXene films show strong reflection up to 90% for the mid-IR wavelengths, resulting in a quite low emissivity. Associated with its high absorption (90%) across the solar spectrum, it achieves a record-high spectral selectivity (8.2) among reported intrinsic solar absorbing materials, and thus the highest solar-thermal conversion efficiency (78% under 1 sun, at 100 °C), to the best of our knowledge. We demonstrated the great potential of this low-emissivity black material in applications that are extremely challenging for traditional rigid metamaterials, including solar-thermal conversion on flexible high-porosity substrates, multispectral camouflage coatings, and anti-counterfeiting. Excellent intrinsic spectral selectivity is offered by $Ti_3C_2T_x$ MXene in a free-standing form as well as coatings on versatile substrates, even on porous rough surfaces, showing much wider applications than metamaterial selective absorbers. The optical properties of the $Ti_3C_2T_x$ MXenes are highly tunable due to the dependence on the terminal groups and the orientation of nanoflakes. Further, first-principles calculations show other commercially available MXenes such as Ti_2CT_x, Nb_2CT_x, and V_2CT_x are also potential low-emissivity black materials, opening the avenue to further exploration of a family of low-emissivity materials with over 70 members.

Results

Low emissivity and high solar absorptance of MXenes. As widely acknowledged, polished metals generally possess high light reflection over an ultra-broad band due to their high damping constant and low refractive index (Fig. 1a). For instance, as shown in Fig. 1b, the stainless steel (SLS) has both a low

solar absorptance of 38% and a low IR emissivity of 9% at 100 °C. In contrast, most of the black materials such as carbon-based absorbers have strong UV-visible-IR absorption (Fig. 1c). A black absorber made of carbon nanotubes (CNT) shows not only a as high as 95%, but also a near-unity of 93% (Fig. 1d). The blackbody-like absorber is not an ideal solar absorber, since most of the harvested solar energy will be dissipated via the massive thermal re-radiation (at 100 °C), leading to a low solar-thermal efficiency $h_{solar\text{-}th}$ of only ~32% under the illumination of 1 sun (1 kW m^{-2}) near room temperature.

Unlike metals and blackbodies, a free-standing 15-mm-thick $Ti_3C_2T_x$ MXene film exhibits a high of 90% comparable to that of the CNT absorber, while beyond the solar spectrum, its absorption rapidly declines to a rather low level due to the increasing mid-IR reflection (Figs. 1e, f). Its is only around 17% at 100 °C, suggesting excellent spectral selectivity ( ). Moreover, the of the $Ti_3C_2T_x$ film can be further reduced to as low as 10% by controlling the surface morphology as discussed later, which is even close to that of some polished metals (9% for W and SLS) (Fig. 1h). To visually demonstrate the low of the $Ti_3C_2T_x$ film, it was placed on a hot plate with a constant temperature of 100 °C, and characterized by an IR imager (the default emissivity was set as 95% in this work). Despite the identical real temperature of 100 °C, the $Ti_3C_2T_x$ film appears much colder than the CNT absorber in the IR image, and as cold as the polished SLS with a comparably low (Fig. 1i). The $h_{solar\text{-}th}$ (1 sun, 100 °C) of the low-emissivity $Ti_3C_2T_x$ film can reach a record-high value of 78% for intrinsic black materials, far higher than that of the CNT absorber (32%). To the best of our knowledge, both the and $h_{solar\text{-}th}$ of the $Ti_3C_2T_x$ MXene are the highest among all the intrinsic solar absorbing materials (> 50%) reported so far (Supplementary Table 1). By virtue of the higher $h_{solar\text{-}th}$, its measured surface temperature rise (62 °C) is higher than that of the CNT absorber (50 °C) under 1-sun illumination in the open air (Fig. 1g).

Fabrication and characterizations of $Ti_3C_2T_x$ MXene films. The free-standing black $Ti_3C_2T_x$ MXene film with great flexibility in this work was prepared by a typical process reported previously[35,37], which includes chemically etching of the Al atoms from Ti_3AlC_2 phases, nanoflakes delamination by centrifugation, and vacuum-assisted filtration. The TEM image of the prepared $Ti_3C_2T_x$ powder after delamination verifies that 2D nanoflakes with few layers were attained (Fig. 2a). The cross-sectional SEM image of the filtrated film shows that it has a 15 μm thickness and is stacked by well-aligned nanoflakes (Fig. 2b). Both the X-ray diffraction (XRD) and the X-ray photoelectron spectroscopy (XPS) were performed to characterize the vacuum-filtrated $Ti_3C_2T_x$ film (the top side). The XRD pattern with a pronounced peak at 2θ = 6.5° is assigned to the (002) plane of the $Ti_3C_2T_x$ MXene (Fig. 2c), which is well consistent with the results in the previous works[37,42]. Moreover, the XPS results verify the presence of Ti, C, O, and F in the film, with a percentage atomic composition of 22.8%, 42.4%, 26.3%, and 8.5%, respectively (Fig. 2d). The high-resolution XPS spectra of O, F, Ti, and C are deconvoluted to analyze their valence states and the terminal groups of the film (Figs. 2e, f and Supplementary Fig. 1). Three types of terminal groups are identified in the $Ti_3C_2T_x$ film including oxide (-O-), hydroxyl (-OH), and fluoride (-F), where both -OH and -O- account for the majority.

Both the top and bottom surfaces of the $Ti_3C_2T_x$ film show strong light absorption for the wavelengths from 0.3 to 1.2 μm and dramatically reduced absorption for longer wavelengths (Fig. 2g and Supplementary Fig. 2). The superior performance can be maintained without notable decay after long-term (120 hours) thermal annealing in both the vacuum (< 7×10^{-2} Torr) at 400 °C and the ambient air at 200 °C (Supplementary Fig. 3). Interestingly, the absorption of the top surface is slightly higher than that of the bottom over the whole spectral range. The and @100 °C of the top are 90% and 17%, while those of the bottom are 82% and 10%, respectively. As a result, although with the same surface temperature (~100 °C), the bottom (39 °C) appears a bit colder than the top (45 °C) in the IR image (Fig. 2h). The surface SEM images reveal that the bottom surface that adhered to the filter membrane during filtration is flatter than the top (Fig. 2i). Their 3D morphologies given by a surface profiler also quantitatively verify the roughness of the bottom surface (R_a = 215 nm) is around half of that for the top surface (410 nm) (Supplementary Figs. 4 and 5). This difference in morphology is attributed to the different boundary conditions of the two surfaces during vacuum-assisted filtration. The stacking of nanoflakes in the bottom was assisted by the flat filter membrane and strong vacuum pressure, while the top surface was formed under weaker constraints. In other words, some of the nanoflakes on top were not oriented parallel to the filter membrane during filtration and formed a rougher surface. Here we infer that the in-plane and cross-plane optical properties of the 2D MXene nanoflakes differ from each other. Consequently, the variations in the 2D nanoflakes orientation will lead to the discrepancy in absorption properties between the two surfaces.

To test this hypothesis, we simply coated the $Ti_3C_2T_x$ solution on two different substrates including silicon and glass by drop-casting to obtain more randomly oriented nanoflakes. The absorption intensity of both the two films over the UV-visible-IR range is stronger than that of the vacuum-filtrated film, indicating larger and (Supplementary Fig. 6a). From the cross-sectional SEM image of the film on silicon (Supplementary Fig. 6b), we observed that the majority of nanoflakes are stacked together with random orientations, which is different from the well-aligned architecture of the vacuum-filtrated film (Fig. 2a). There are a lot of bumps on the film surface and the roughness is quite large (Inset of Supplementary Fig. 6b). These phenomena confirm the strong dependence of the optical properties on the orientation of nanoflakes. The fundamental reason is that the in-plane permittivity of the 2D MXenes differs from the cross-plane permittivity. Actually, for the MXene films prepared by different approaches, variations in the geometry and therefore in the electrical conductivity were also reported in prior works[43,44]. Even with randomly oriented nanoflakes, the films still offer a much lower of 45% than the CNT absorber. Therefore, accompanied by a high of 92%, their $h_{solar\text{-}th}$ is still superior to CNT absorbers.

Potential applications of low-emissivity black MXenes. Porous structures are indispensable components to a lot of solar-thermal applications, such as steam generation[1], seawater desalination[39], and smart textiles[45]. However, current high-performance selective solar absorbers are usually realized by constructing artificial metamaterials/metasurfaces in nanoscale (multilayer nanofilms or nanophotonic structures) on dense flat substrates[2-4,24,26], which will lose their effectiveness when coated on porous substrates owing to the break of resonant conditions. For instance, we coated a previously reported high-

performance metamaterial absorber (Ag film/TiN nanoparticles/SiO_2) on a highly porous Nylon 66 membrane shown in the inset of Fig. 3a. The metamaterial absorber only offers a low of 45%, much lower than the values (~95%) on dense substrates[3]. In contrast, the intrinsic $Ti_3C_2T_x$ sustained its high of 85% and low of 25% even on highly porous membranes (Fig. 3a), because its optical properties are dominated by the material itself instead of the subwavelength microstructures. As a result, the $h_{solar\text{-}th}$ of the $Ti_3C_2T_x$-Nylon 66 absorber (68% under 1 sun, at 100 °C) is superior to that of its metamaterial-based counterpart (42%).

Under the COVID-19, discarded face masks made from long-lasting plastics have been becoming a disaster to the environment. Moreover, the disposal of masks without disinfection may cause further virus transmission. The efficient $Ti_3C_2T_x$ absorber on porous Nylon 66 is promising to be used in disinfecting of face masks under solar illumination and make masks reusable. As shown in Fig. 3b, under the exposure of 1 sun, the N95 face mask with $Ti_3C_2T_x$-Nylon 66 was rapidly heated to the critical temperature of 70 °C for virus inactivation within 1 min[46,47]. After 10 min exposure, the surface temperature of the face mask reached around 90 °C, while that of the metamaterial-based mask was only 72 °C due to the lower $h_{solar\text{-}th}$.

In short, intrinsic MXene absorbers are compatible with both dense and porous substrates, and can also work in the form of a free-standing film, which significantly expands application scenarios of selective solar absorbers. Moreover, unlike metamaterials, there is no need to employ time-consuming, expensive nanofabrication techniques for the preparation of such intrinsic absorbers, which make them more attractive in large-scale applications.

Besides the solar-thermal conversion, the low-emissivity black MXenes can benefit many other areas such as multispectral camouflage and anti-counterfeiting. In conventional IR camouflage coatings that are mostly made of metallic micro powders such as aluminum, both the high glossiness and high brightness limit their compatibility with visible and even near-IR light[22,48]. Figs. 3c and d show the optical and IR images of a person who wore a white T-shirt with black $Ti_3C_2T_x$ coating (0.16×0.128 m^2) at night. The temperature reading of the area with $Ti_3C_2T_x$ coating in the IR image was only 25 °C and much lower than the body temperature (~36 °C), appearing nearly as cold as the environment (23 °C). This result demonstrates that low-emissivity $Ti_3C_2T_x$ could be implemented as IR camouflage coatings to conceal human bodies from IR detection. Meanwhile, as shown in Fig. 3c, the black $Ti_3C_2T_x$ coating on the white T-shirt was invisible at night, allowing the covered objects to blend in with the dark environment. In other words, the low-emissivity black $Ti_3C_2T_x$ can overcome the issues of conventional IR camouflage coatings and be an appealing alternative in both IR and visible camouflage.

Counterfeiting is causing tremendous losses in both the security and property of customers, companies, and governments. Anti-counterfeiting features are increasingly demanded to prevent valuable items such as brands, tickets, quick response (QR) codes, banknotes, and confidential documents from being replicated. Currently, most anti-counterfeiting technologies are enabled by photoluminescence[49] and

magnetic response[50]. Here we demonstrated an alternative technology against counterfeiters by using IR-metameric security inks composed of low-emissivity MXenes. In Fig. 3e, the black anti-counterfeiting word “HKUST” was written on a white (polyvinylidene fluoride) PVDF membrane using both the commercial black paint (for “HK”) and the $Ti_3C_2T_x$ MXene solution (for “UST”), which cannot be told apart by naked eyes because of the similar spectral features in visible light. However, the “HK” almost disappeared under the IR thermal imager due to the small contrast in of the PVDF (~95%) and the black paint (~92%), while the “UST” can still be clearly observed because of the much lower of the $Ti_3C_2T_x$ (Fig. 3f).

Theoretical investigations. To explore the underlying mechanisms of the spectral selectivity in the $Ti_3C_2T_x$, and search for more potential low-emissivity MXenes, we investigated their optical properties by the density functional theory (DFT) calculations. As shown in Fig. 4a, bulk $Ti_3C_2T_x$ films made of layered flakes with and without different terminal groups (-OH, -O, and -F) under the normal incidence of light were calculated. Referring to the Fresnel equation, the surface light reflection (R) from materials in the air at normal incidence can be obtained by

$$r(\omega)=\left|\frac{\sqrt{\varepsilon_1(\omega)+i\varepsilon_2(\omega)}-1}{\sqrt{\varepsilon_1(\omega)+i\varepsilon_2(\omega)}+1}\right|^2 \qquad (1)$$

where ω is the angular frequency and is the permittivity. Then, for optically thick materials with no transmission, the light absorption can be expressed as

$$\alpha(\omega)=1-r(\omega) \qquad (2)$$

Large ε_1 or ε_2 values lead to high surface reflection, and therefore low absorption/emission. On the contrary, to achieve low reflection and therefore high absorption, ε_1 nd ε_2 should approach 1 and 0 ($\varepsilon_2 >$ 0). It should be noted that at normal incidence (wave vector along the z-direction), the electric component of light orients in the x-y plane (Fig. 4a). Hence, it is the in-plane permittivity that dominates the reflection. Interestingly, for the four kinds of $Ti_3C_2T_x$, both the in-plane ε_1 and ε_2 are relatively smaller in the UV-visible-NIR range but increase to quite large levels in the mid-IR region (Figs. 4b, c). As a result, they offer wavelength selectivity in light absorption as expected (Fig. 4d). In particular, both the $Ti_3C_2(OH)_2$ and the $Ti_3C_2F_2$ exhibit high solar absorptance and low IR emissivity. Moreover, the DFT results verify that the in-plane permittivity of the $Ti_3C_2T_x$ MXenes is different from that along the z-direction. This well explains why the absorption properties of the films strongly depend on the orientations of nanoflakes. As shown in Fig. 4g and Supplementary Fig. 7, for $Ti_3C_2T_x$ with various terminal groups, their absorptance calculated from the in-plane permittivity shows much better spectral selectivity than that from the z-direction, indicating that well-aligned nanoflakes parallel to the substrate

are preferable, which is consistent with the experiments. Due to the differences in composition, the absorption spectra of the $Ti_3C_2T_x$ given by the DFT calculations do not exactly agree with the experimental data. However, they validate the great spectral selectivity, and demonstrate the dependences on terminal groups and nanoflake orientations. Apart from the $Ti_3C_2T_x$, the DFT calculations suggest that other MXenes such as Ti_2CT_x, Nb_2CT_x, and V_2CT_x are also promising low-emissivity black materials (Fig. 4h and Supplementary Fig. 8).

Discussion

In summary, we for the first time report on a group of 2D MXenes as black materials with low emissivity. It is demonstrated that the free-standing $Ti_3C_2T_x$ film prepared by vacuum-assisted filtration offers both a high solar absorptance up to 90% and a low IR emissivity down to 10%, yielding the highest spectral selectivity for intrinsic solar absorbing materials reported so far. As a result, under 1 sun illumination in the open air, the MXene film achieves a high temperature rise around 62 °C with respect to the ambient air. By comparison, the temperature of the CNT absorber with a higher emissivity only increases by 50 °C, due to the higher photo-thermal conversion efficiency provided by the lower emissivity. Both our experiments and DFT calculations reveal that the absorption/emission properties of the MXenes strongly rely on the orientation of the nanoflakes, and the terminal groups. Specifically, lower emissivity is obtained in those films with nanoflakes well-aligned parallel to the substrates, and -OH and/or -F terminal groups. The highly selective, flexible, black MXenes show great potential in solar-thermal energy conversion, IR camouflage, thermal insulation, and anti-counterfeiting.

Methods

Fabrication of the MXene films. The $T_{i3}C_2T_x$ colloidal solution was prepared by the liquid-phase delamination of Ti_3AlC_2 powder. In detail, 1.98 g of lithium fluoride (LiF) (Alfa Aesar, 98.5%) was added to 35 mL of 9 M HCl aqueous solution. Then, 2 g of Ti_3AlC_2 powder was added to the mixture. After etching for 24 h at 35 °C, the solution was washed and centrifuged with deionized water until the supernatant reached a pH value of 6. Next, to delaminate the MXene, 1 g etched MXene was dispersed into 0.5 L DI water, and deaerated with Ar, followed by sonication for 1 h. The mixture was then centrifuged for 1 h at 3500 rmp, and the supernatant with dark green color was collected. After that, a certain amount of MXene dispersion solution was vacuum filtrated through a hydrophilic Celgard 3501 membrane, and the obtained MXene membrane was further dried under 60 °C in the vacuum oven, and a membrane with a thickness of about 15 μm was obtained. The concentration of the solution was determined by testing the weight of the dried MXene film.

Material characterizations. The morphology of the $Ti_3C_2T_x$ nanoflakes was observed by transmission electron microscopy (TEM, JEM-2010F, Jeol). The phase identification of the MXene film was conducted by using an X-ray diffractometer (XRD, PANalytical) with Cu Kα radiation at 45 kV and 40 mA. The surface and cross-section morphologies were characterized by scanning electron microscopy (SEM, JSM-7100F,

Jeol) equipped with energy dispersive X-ray spectroscopy (EDX). The composition of the film was characterized by X-ray photoelectron spectroscopy (XPS, PHI 5600 multi-technique system, Physical Electronics). A 3D optical profiler (NPFLEX, Bruker) was used to characterize the morphology and roughness of the film. The surface roughness was obtained by analyzing 307,200 data points with a vertical resolution of 0.15 nm.

Optical measurements. The UV-visible-NIR (0.3-2.5 μm) reflectance (*R*) and transmittance (*T*) spectra of the samples were measured using a spectrometer (Lambda 950, Perkin Elmer) equipped with a 150 mm integrating sphere. A white $BaSO_4$ plate was used as a standard reference in the UV-visible-NIR reflectance measurements. The mid-IR (MIR, > 2.5 μm) *R* and *T* spectra were measured using a Fourier transform infrared spectrometer (FTIR, Vertex 70, Bruker) with an integrating sphere. A gold film was used as a standard reference in the mid-IR reflectance measurements. The absorptance (*A*) spectra were directly derived from 1-*R*-*T*.

Thermal measurements. To measure the temperature rise under solar illumination, the MXene film and reference samples were attached to the surface of polystyrene foam. A solar simulator (Oriel Sol2A, Newport) using a xenon lamp was used to provide standard and stable 1-sun power (1 kW m^{-2}). T-type thermal couples, which were connected to a data acquisition device (NI9213, National Instrument), were attached on the backside of samples to measure the steady-state temperatures. The temperature data were recorded every two seconds. A thermal imager (Ti25, Fluke) was used to taken IR photos of the samples.

Solar absorptance and thermal emissivity calculation. The spectrally averaged solar absorptance $\bar{\alpha}$ is defined as[2]

Solar absorptance and thermal emissivity calculation. The spectrally averaged solar absorptance $\bar{\alpha}$ is defined as[2]

$$\bar{\alpha} = \frac{\int_{0.3\mu m}^{4\mu m} \alpha(\lambda) E_{solar}(\lambda) d\lambda}{I_{solar}} \quad (3)$$

The spectrally averaged thermal emissivity $\bar{\varepsilon}$ is calculated by[2]

$$\bar{\varepsilon}(T) = \frac{\int_{0.3\mu m}^{20\mu m} \varepsilon(\lambda) E_b(\lambda, T) d\lambda}{\sigma T^4} \quad (4)$$

Here $E_{solar}(\lambda)$, $E_b(\lambda,T)$, $\alpha(\lambda)$, and $\varepsilon(\lambda)$ represent the spectral solar power (AM 1.5G), the blackbody emission at *T*, the absorptance, and the emissivity at the wavelength λ, respectively. I_{solar} is the total solar irradiance (AM 1.5G, 1 sun or 1 kW m^{-2}), and σ is the Stefan-Boltzmann constant.

Solar-thermal conversion efficiency calculation. The solar-thermal energy conversion efficiency under 1 sun can be obtained by[2]

$$\eta_{solar-th}(T) = \bar{\alpha} - \bar{\varepsilon}\frac{\sigma(T^4 - T_0^4)}{I_{solar}} \quad (5)$$

where T is the operating temperature, and T_0 is the ambient temperature.

Thermal stability tests. Thermal annealing cycles (24 hours × 5 cycles) in ambient air at both 100 and 200 °C were conducted by placing the samples on a hot plate (KW-4AH, Chemat Technology Inc.). Thermal annealing cycles (24 hours × 5 cycles) in vacuum at both 300 and 400 °C were conducted in a quartz tube furnace (OTF-1200X, MTI Corporation). The samples placed in a ceramic crucible were put in the quartz tube and sealed. The sealed quartz tube was evacuated to reach a vacuum atmosphere (<7×10^{-2} Torr). Afterward, the samples were heated up to 300 °C (or 400 °C) at a rate of 10 °C/min and annealed for 24 h $cycle^{-1}$.

Data availability

The data sets generated and analyzed during the current study are available from the corresponding author upon reasonable request.

Declarations

Acknowledgements

The authors would like to acknowledge for the financial support from the Hong Kong General Research Fund (Grant No. 16214217) and the Hong Kong Collaborative Research Fund (C6022-16G). D.M. and Y.L. also acknowledge the financial support from the National Natural Science Foundation of China (No. 52075484).

Author contributions

Y.L. and B.H. conceived and designed the research. C.X., Y.L. and X.P. performed the sample fabrication. Y.L., M.L. and C.X. conducted the material characterization and optical measurements. Y.L., G.L. and M.L. performed the demonstrations of potential applications. H.H. performed the DFT calculation. Y.L., C.X., H.H., D.M., M.W., T.Z. and B.H. analyzed the results and wrote the manuscript. All authors approved the final version of the manuscript.

Additional information

Supplementary Information is available for this paper at

Competing interests: The authors declare no competing interests.

References

1 Ni, G. et al. Steam generation under one sun enabled by a floating structure with thermal concentration. *Nat. Energy* **1,** 16126 (2016).

2 Cao, F., McEnaney, K., Chen, G. & Ren, Z. F. A review of cermet-based spectrally selective solar absorbers. *Energy Environ. Sci.* **7,** 1615-1627 (2014).

3 Li, Y. et al. Solution-processed all-ceramic plasmonic metamaterials for efficient solar–thermal conversion over 100–727 °c. *Adv. Mater.* **33,** 2005074 (2021).

4 Lin, K.-T., Lin, H., Yang, T. & Jia, B. Structured graphene metamaterial selective absorbers for high efficiency and omnidirectional solar thermal energy conversion. *Nat. Commun.* **11,** 1389 (2020).

5 Jelle, B. P., Kalnaes, S. E. & Gao, T. Low-emissivity materials for building applications: A state-of-the-art review and future research perspectives. *Energ Buildings* **96,** 329-356 (2015).

6 Zhang, Z. T. et al. Solution-based fabrication of vanadium dioxide on f:Sno2 substrates with largely enhanced thermochromism and low-emissivity for energy-saving applications. *Energy Environ. Sci.* **4,** 4290-4297 (2011).

7 Zhu, H. et al. High-temperature infrared camouflage with efficient thermal management. *Light: Science & Applications* **9,** 60 (2020).

8 Kim, T., Bae, J. Y., Lee, N. & Cho, H. H. Hierarchical metamaterials for multispectral camouflage of infrared and microwaves. *Adv. Funct. Mater.* **29** (2019).

9 Li, Y. G. et al. Selective light absorber-assisted single nickel atom catalysts for ambient sunlight-driven co2 methanation. *Nat. Commun.* **10,** 2359 (2019).

10 Ghasemi, H. et al. Solar steam generation by heat localization. *Nat. Commun.* **5,** 4449 (2014).

11 Chen, C. J. et al. Highly flexible and efficient solar steam generation device. *Adv. Mater.* **29,** 1701756 (2017).

12 Li, X. Q. et al. Graphene oxide-based efficient and scalable solar desalination under one sun with a confined 2d water path. *Proc. Natl. Acad. Sci. USA* **113,** 13953-13958 (2016).

13 Zhao, F. et al. Highly efficient solar vapour generation via hierarchically nanostructured gels. *Nat. Nanotechnol.* **13,** 489-495 (2018).

14 Moon, J. et al. Black oxide nanoparticles as durable solar absorbing material for high-temperature concentrating solar power system. *Sol. Energy Mater. Sol. Cells* **134,** 417-424 (2015).

15 Wang, J. et al. High-performance photothermal conversion of narrow-bandgap ti2o3 nanoparticles. *Adv. Mater.* **29,** 1603730 (2017).

16 Feng, K. et al. Cobalt plasmonic superstructures enable almost 100% broadband photon efficient co2 photocatalysis. *Adv. Mater.* **32,** 2000014 (2020).

17 Li, X. et al. Integration of daytime radiative cooling and solar heating for year-round energy saving in buildings. *Nat. Commun.* **11,** 6101 (2020).

18 Dash, S., de Ruiter, J. & Varanasi, K. K. Photothermal trap utilizing solar illumination for ice mitigation. *Sci. Adv.* **4,** eaat0127 (2018).

19 Ma, P. J. et al. Spinel-type solar-thermal conversion coatings on supercapacitors: An effective strategy for capacitance recovery at low temperatures. *Energy Storage Materials* **23,** 159-167 (2019).

20 Tu, S. B. et al. Autonomous mxene-pvdf actuator for flexible solar trackers. *Nano Energy* **77** (2020).

21 Weinstein, L. A. et al. Concentrating solar power. *Chem. Rev.* **115,** 12797-12838 (2015).

22 Yan, X. X., Wang, L. & Qian, X. Y. Preparation and characterization of low infrared emissive aluminum/waterborne acrylic coatings. *Coatings* **10,** 35 (2020).

23 Rinnerbauer, V. et al. Metallic photonic crystal absorber-emitter for efficient spectral control in high-temperature solar thermophotovoltaics. *Adv. Energy. Mater.* **4,** 1400334 (2014).

24 Li, P. et al. Large-scale nanophotonic solar selective absorbers for high-efficiency solar thermal energy conversion. *Adv. Mater.* **27,** 4585-4591 (2015).

25 Mandal, J. et al. Scalable, “dip-and-dry” fabrication of a wide-angle plasmonic selective absorber for high-efficiency solar–thermal energy conversion. *Adv. Mater.* **29,** 1702156 (2017).

26 Li, Y. et al. Scalable all-ceramic nanofilms as highly efficient and thermally stable selective solar absorbers. *Nano Energy* **64,** 103947 (2019).

27 Wu, Z. X. et al. Enhanced spectral selectivity through the quasi-optical microcavity based on w-sio2 cermet. *Mater. Today Phys.* **9,** 100089 (2019).

28 Wang, X. Y. et al. High-temperature tolerance in wti-al_2o_3 cermet-based solar selective absorbing coatings with low thermal emissivity. *Nano Energy* **37,** 232-241 (2017).

29 Guo, H. X. et al. A novel multilayer high temperature colored solar absorber coating based on high-entropy alloy monbhfzrti: Optimized preparation and chromaticity investigation. *Sol. Energy Mater. Sol. Cells* **209,** 110444 (2020).

30 Kennedy, C. E. Review of mid- to high-temperature solar selective absorber materials. (United States, 2002).

31 Sani, E. et al. Spectrally selective ultra-high temperature ceramic absorbers for high-temperature solar plants. *J Renew Sustain Ener* **4,** 033104 (2012).

32 Sani, E. et al. Titanium diboride ceramics for solar thermal absorbers. *Sol. Energy Mater. Sol. Cells* **169,** 313-319 (2017).

33 Naguib, M. et al. Two-dimensional nanocrystals produced by exfoliation of ti3alc2. *Adv. Mater.* **23,** 4248-4253 (2011).

34 Anasori, B., Lukatskaya, M. R. & Gogotsi, Y. 2d metal carbides and nitrides (mxenes) for energy storage. *Nat Rev Mater* **2,** 16098 (2017).

35 Xiong, C. et al. Achieving multiplexed functionality in a hierarchical mxene-based sulfur host for high-rate, high-loading lithium-sulfur batteries. *Energy Storage Materials* **33,** 147-157 (2020).

36 Gao, G. P., O'Mullane, A. P. & Du, A. J. 2d mxenes: A new family of promising catalysts for the hydrogen evolution reaction. *Acs Catal.* **7,** 494-500 (2017).

37 Shahzad, F. et al. Electromagnetic interference shielding with 2d transition metal carbides (mxenes). *Science* **353,** 1137-1140 (2016).

38 Liu, J. et al. Hydrophobic, flexible, and lightweight mxene foams for high-performance electromagnetic-interference shielding. *Adv. Mater.* **29,** 1702367 (2017).

39 Li, R. Y., Zhang, L. B., Shi, L. & Wang, P. Mxene ti3c2: An effective 2d light-to-heat conversion material. *ACS Nano* **11,** 3752-3759 (2017).

40 Lin, H. et al. Two-dimensional ultrathin mxene ceramic nanosheets for photothermal conversion. *Nano Lett.* **17,** 384-391 (2017).

41 Maleski, K., Mochalin, V. N. & Gogotsi, Y. Dispersions of two-dimensional titanium carbide mxene in organic solvents. *Chem Mater* **29,** 1632-1640 (2017).

42 Shah, S. A. et al. Template-free 3d titanium carbide (ti3c2tx) mxene particles crumpled by capillary forces. *Chem Commun* **53,** 400-403 (2017).

43 Pomerantseva, E. & Gogotsi, Y. Two-dimensional heterostructures for energy storage. *Nat. Energy* **2,** 17089 (2017).

44 Zhang, J. Z. et al. Scalable manufacturing of free-standing, strong ti3c2tx mxene films with outstanding conductivity. *Adv. Mater.* **32,** 2001093 (2020).

45 Peng, Y. C. & Cui, Y. Advanced textiles for personal thermal management and energy. *Joule* **4,** 724-742 (2020).

46 Kumar, S. et al. Photoactive antiviral face mask with self-sterilization and reusability. *Nano Lett.* **21,** 337-343 (2021).

47 Zhong, H. et al. Reusable and recyclable graphene masks with outstanding superhydrophobic and photothermal performances. *ACS Nano* **14,** 6213-6221 (2020).

48 Wu, G. W. & Yu, D. M. Preparation and characterization of a new low infrared-emissivity coating based on modified aluminum. *Prog Org Coat* **76,** 107-112 (2013).

49 Jiang, K. et al. Triple-mode emission of carbon dots: Applications for advanced anti-counterfeiting. *Angew. Chem. Int. Edit.* **55,** 7231-7235 (2016).

50 Hu, H. B., Zhong, H., Chen, C. L. & Chen, Q. W. Magnetically responsive photonic watermarks on banknotes. *J. Mater. Chem. C* **2,** 3695-3702 (2014).

Figures

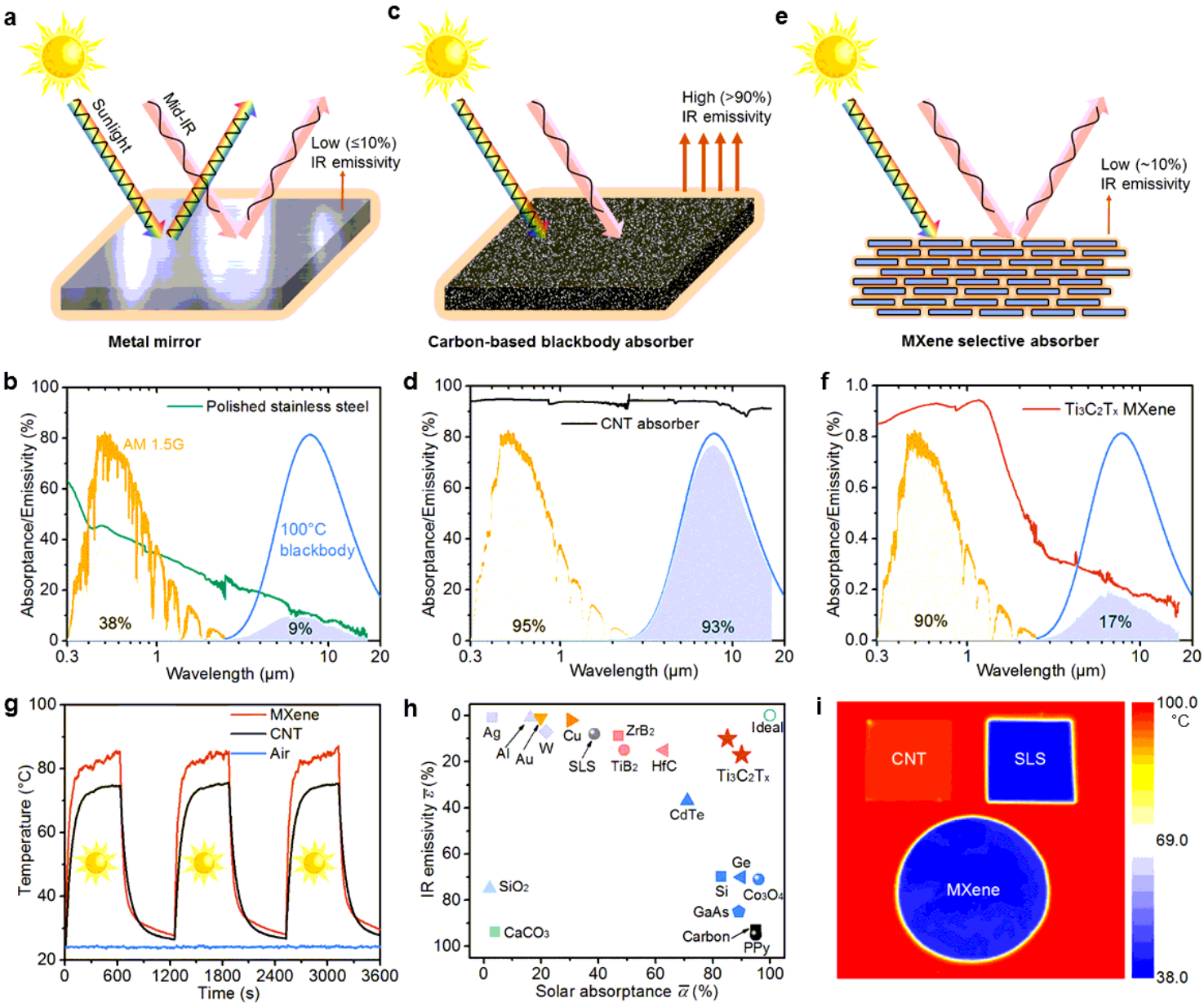

Figure 1

Light-matter interaction of metals, carbon-based blackbodies, and MXenes. a, The high solar reflectance, high mid-IR reflectance, and low IR emissivity of metals. c, The high solar absorptance, high mid-IR absorptance, and high IR emissivity of carbon-based blackbodies. e, The high solar absorptance, high mid-IR reflectance, and low IR emissivity of MXenes. b,d,f, Absorptance spectra of a polished stainless steel (SLS) sheet, a CNT black absorber, and a Ti3C2Tx MXene film, as well as the AM 1.5G solar spectrum and the radiation spectrum of a blackbody at 100 °C. g, Temperature vs. time of the CNT and MXene absorbers, and the air temperature under 1 sun. h, Comparison of solar absorptance and IR emissivity of intrinsic materials including metals (Au, Ag, Al, Cu, W, and SLS), radiative cooler materials (SiO2 and CaCO3), semiconductors (Si, Ge, CdTe, GaAs, and Co3O4)30, black materials (carbon-based and polymers), TiB232, ZrB232, HfC31, and Ti3C2Tx MXenes. i, IR photographs of the SLS, CNT, and MXene on a hot plate with a constant temperature of 100 °C.

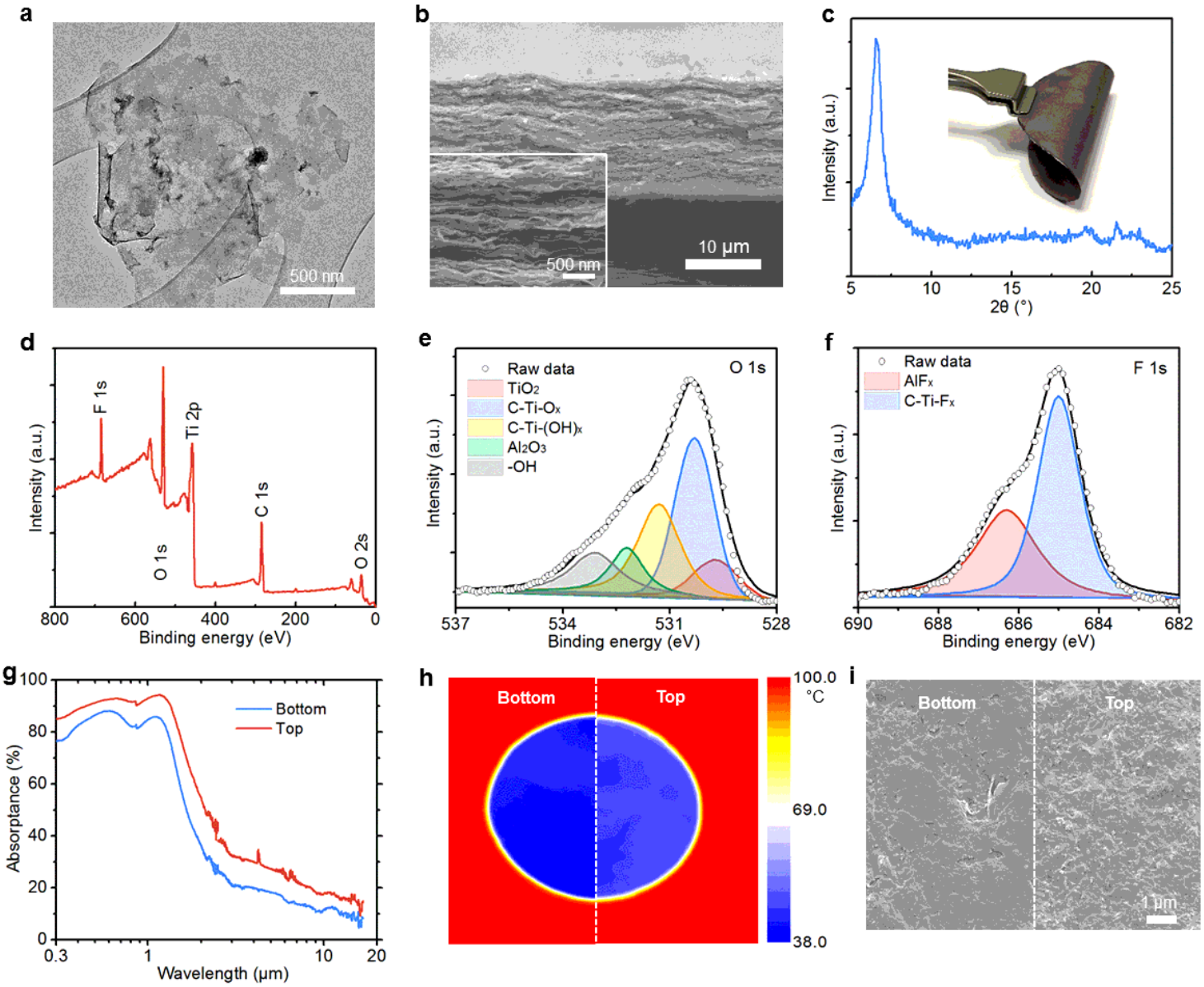

Figure 2

Characterizations of the free-standing Ti3C2Tx MXene film fabricated by vacuum-assisted filtration. a, TEM image of few-layer Ti3C2Tx nanoflakes. b, Cross-sectional SEM image of the free-standing film. c, XRD pattern of the film. Inset: Photograph of the flexible black film (top side). d, XPS spectrum of the film. e,f, High-resolution XPS spectra of O 1s and F 1s of the film. g, Absorptance spectra of the bottom (attached to the filter membrane) and top sides of the vacuum-filtrated film. h, IR photographs of the two sides placed on a hot plate (100 °C). i, Surface SEM images of the two sides.

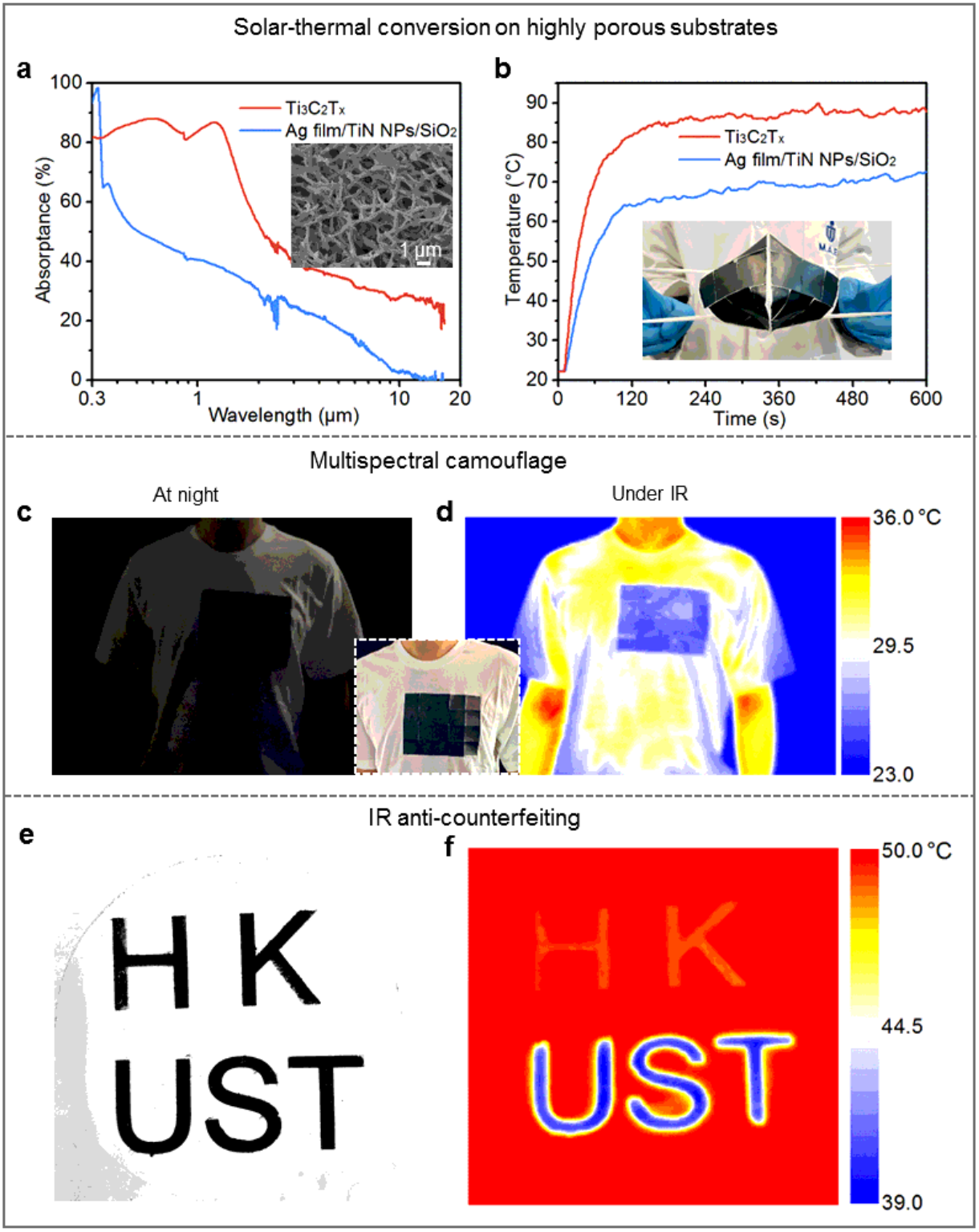

Figure 3

Potential applications of the low-emissivity black Ti3C2Tx. a, Absorptance spectra of highly porous Nylon 66 membranes coated with Ti3C2Tx and metamaterial-based selective absorbers (Ag/TiN nanoparticles/SiO2). Inset: SEM image of the highly porous nylon membrane. b, Temperature vs. time of two face masks with Ti3C2Tx coated, and metamaterials coated Nylon 66 membranes. Inset: An optical photograph of a face mask with Ti3C2Tx-Nylon 66 absorber. c,d, Optical and IR photographs of a person

who wore a white T-shirt with the black Ti3C2Tx coating at night. Inset: An optical photograph at daytime. e,f, Optical and IR photographs of the word “HKUST” written using commercial black paint (for “HK”) and Ti3C2Tx MXene (for “UST”) solutions.

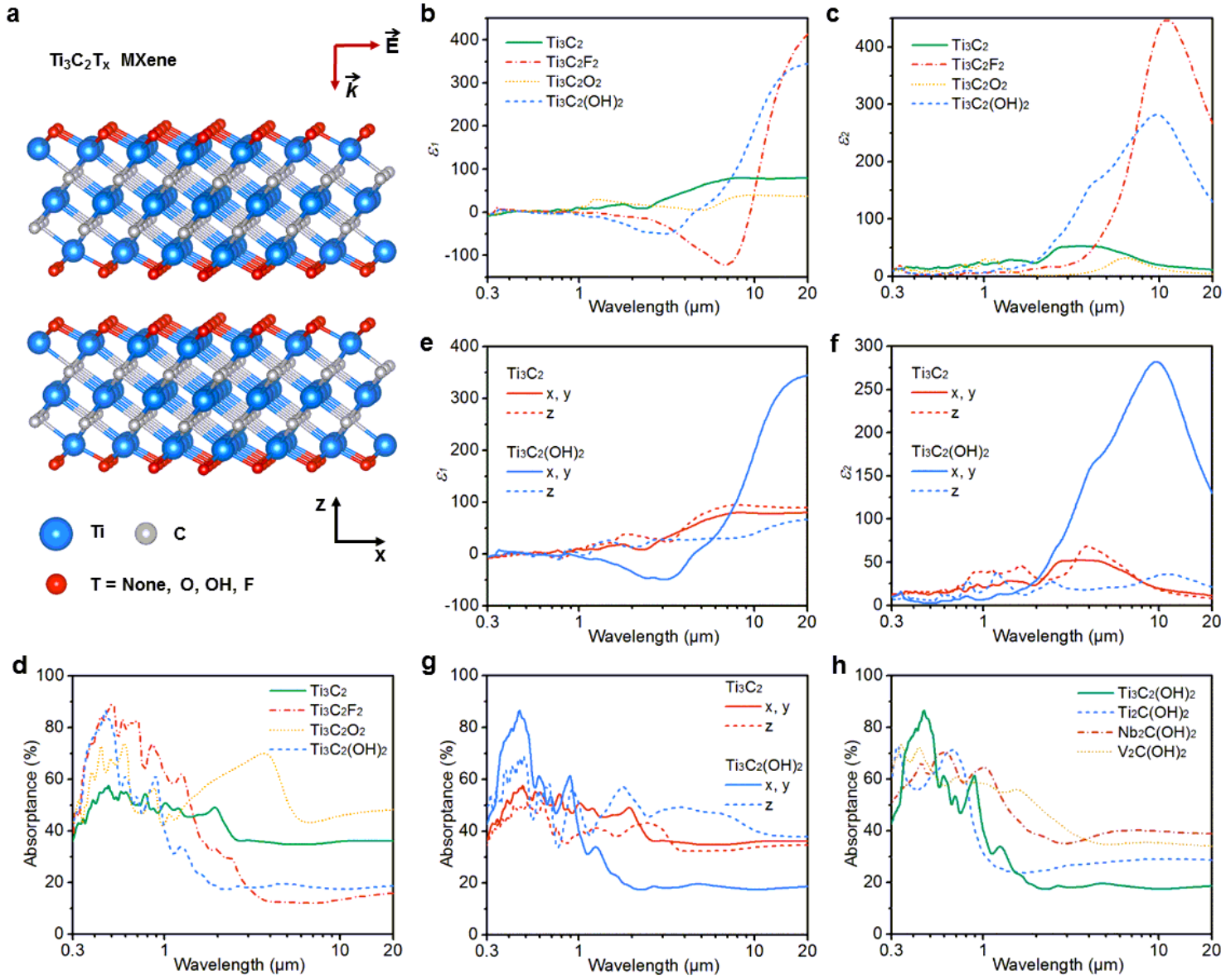

Figure 4

DFT calculations. a, Molecular layered structure of the Ti3C2Tx bulk film. b,c, Real and imaginary parts of in-plane permittivity of the Ti3C2Tx with different groups. d, Calculated absorptance spectra of the Ti3C2Tx with different groups using the in-plane permittivity. e,f, Real and imaginary parts of permittivity of the Ti3C2 and Ti3C2(OH)2 along different directions. g, Calculated absorptance spectra of the Ti3C2 and Ti3C2(OH)2 using permittivity along different directions. h, Calculated absorptance spectra of different MXenes with -OH groups including Ti3C2(OH)2, Ti2C(OH)2, Nb2C(OH)2, and V2C(OH)2, using the in-plane permittivity.

Supplementary Files

This is a list of supplementary files associated with this preprint. Click to download.

- SupplementaryInformation.pdf